

Neural Canonical Transformation for the Spectra of Fluxional Molecule CH_5^+

Ruisi Wang,^{1,2} Qi Zhang,^{1,*} and Lei Wang^{1,†}

¹Beijing National Laboratory for Condensed Matter Physics and Institute of Physics, Chinese Academy of Sciences, Beijing 100190, China

²School of Physical Sciences, University of Chinese Academy of Sciences, Beijing 100190, China

(Dated: February 17, 2026)

Protonated methane, CH_5^+ , is a highly fluxional molecule with large spatial motions of the hydrogen atoms. The molecule's anharmonic effects and the delocalized wavefunction of the hydrogen atoms significantly affect the excitation spectrum of the molecule. The neural canonical transformation (NCT) approach, which we previously developed to solve the vibrational spectra of molecules and solids, is a powerful method that effectively treats nuclear quantum effects and anharmonicities. Using NCT with wavefunctions in atomic coordinates rather than normal coordinates, we successfully calculate the ground and excited states of CH_5^+ . We found that the wavefunctions for the ground state, as well as for low- and high-energy excited states, show preferences for the three stationary points on the potential energy surface. This work extends the applicability of the NCT approach for calculating excited states to fluxional molecules without fixed geometry.

I. INTRODUCTION

Protonated methane, CH_5^+ , is known for its highly fluxional nature [1–4]. It represents the prototypic superacid that plays a pivotal role as a reactive intermediate in acid-catalyzed electrophilic reactions [5, 6], and is also considered a crucial intermediate in the formation of polyatomic organic compounds within cold interstellar clouds [7, 8]. Although initially observed by mass spectroscopy in the early 1950s [9], the first infrared (IR) spectrum of CH_5^+ was not successfully measured until 1999 [10], yet it remained unassigned. Another breakthrough occurred in 2015 with the measurement of experimental combination differences by Asvany et al. [11] (with an improvement reported in Ref. [12]), serving as another key experiment in advancing the understanding of CH_5^+ [13]. The combination difference is the difference of two transition wavenumbers that share a common energy level. Subtracting them cancels the shared level and retrieves the energy spacing of the other two levels.

Concurrent with experimental progress, significant advancements in numerical methods have emerged. An ab initio calculation of the millimeter-wave spectrum of CH_5^+ [14] and an MP2/cc-pVTZ-based potential energy surface (PES) [15] were reported in 2003. In 2004, diffusion Monte Carlo (DMC) techniques were applied to the ground-state calculation of CH_5^+ with an ab initio-based PES [16–18]. Then in 2006, a full-dimensional PES based on CCSD(T)/aug-cc-pVTZ data that could successfully capture the dissociation process of CH_5^+ was reported [19], becoming the state-of-the-art PES of CH_5^+ since then. Subsequently, researchers have applied various methods to investigate the (ro-)vibrational excited states and the infrared spectrum of CH_5^+ and its isotopologs. These include large-scale vibrational configuration interaction (VCI) calculations [20, 21], DMC methods [22–24], contracted basis-iterative method [25–28], (multilayer) multiconfigurational time-dependent Hartree method [29], the

molecule superrotor model method [30, 31], and the quantum-graph (QG) model [32–35]. Despite significant advances in experimental and computational methods, the accurate assignment of spectral lines for CH_5^+ remains an unsolved problem. Consequently, considerable effort is still required to interpret its spectrum and elucidate the molecule's complex dynamics.

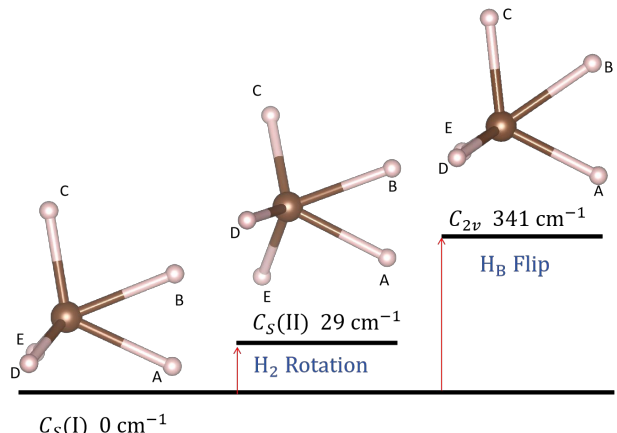


Figure 1. The structures of the three stationary points on the CH_5^+ PES with energies relative to the global minimum at the CCSD(T) level from Ref. [21]. In the C_s (I) configuration, the hydrogens A, B, and C lie in the same plane as the central carbon. D and E are positioned symmetrically with respect to this plane. The H_2 moiety is formed by A and B. In the C_s (II) configuration, the H_2 moiety (also formed by A and B) is rotated by 30° relative to the C_s (I) configuration, and another 30° rotation of the H_2 moiety would lead back to another C_s (I) configuration. In the C_{2v} configuration, the hydrogens labeled A and C are symmetric with respect to the plane formed by D, B, E, and the central carbon.

The addition of a proton to methane (CH_4) to form CH_5^+ causes a significant structural deviation from the tetrahedral geometry of methane. The relatively rigid structure of CH_4 creates high energy barriers that prevent the free permutation of its hydrogen atoms during molecular vibration. This allows each hydrogen atom to be uniquely labeled. An equilibrium

* zhangqi94@iphy.ac.cn

† wanglei@iphy.ac.cn

geometry with an arbitrary but fixed numbering of the atoms can be chosen as a reference configuration. During vibration, the molecule primarily explores regions of the PES near this reference geometry [36, 37]. Because the dynamics are localized in this manner, analyses based on normal coordinates are both appropriate and successful [38–40]. In contrast, the PES of CH_5^+ features 120 equivalent minima that differ from one another only by the permutation of hydrogen atoms. These minima are interconnected by low-energy barriers, causing the ground-state wavefunction to be delocalized over all 120 configurations. Adjacent minima on the PES are connected by stationary points of different symmetries. Starting from a global minimum with $C_s(\text{I})$ symmetry, a $C_s(\text{II})$ stationary point is accessed via a 30° rotation of the H_2 moiety. Alternatively, a flip motion that exchanges hydrogens between the H_2 and the CH_3 components proceeds through a C_{2v} stationary point (see Fig. 1, visualized by VESTA [41]). Both stationary points represent low energy barriers relative to the global minimum: the barrier height is only 29 cm^{-1} for the $C_s(\text{II})$ point and 341 cm^{-1} for the C_{2v} point. The resulting fluxionality of CH_5^+ produces a complex energy level structure across its spectrum. A prime example is the 175 cm^{-1} level, which is assigned to a highly anharmonic H_B flip isomerization [21]—a large-amplitude motion with no counterpart in the spectrum of rigid CH_4 . Furthermore, approximately 900 spectral lines are observed in the 2770–3150 cm^{-1} region, as reported in Ref. [10], which significantly exceeds the number of spectral lines found in that region for CH_4 and CH_5^+ [42].

The application of machine learning methods to the computation of the PES and (ro-)vibrational energy levels has recently gained significant attention as an emerging trend [43–53]. Among these methods, the neural canonical transformation (NCT) [43] is a notable variational approach for the scalable and simultaneous computation of multiple excited states. The method begins with an initial set of orthogonal basis functions and employs a neural network to transform this basis into the optimum wavefunctions. This transformation is designed to strictly preserve orthogonality. A key advantage of NCT is that it provides direct access to the wavefunctions, which simplifies the calculation of physical properties. The NCT approach has been successfully applied to various systems, including the thermal properties of interacting fermions [54], the effective mass of interacting electrons [55], the equation of state of dense hydrogen in extreme situations [56], the quantum anharmonic effects of quantum solids [57], the vibrational eigenstates of molecules [43] and the high-pressure water ice [58].

The primary objective of this paper is to apply the NCT method to compute the ground and excited eigenstates of the highly fluxional molecule CH_5^+ . Our previous implementation of NCT [43] used normal coordinates, which are unsuitable for a highly fluxional system like CH_5^+ , whose wavefunction is delocalized over many equivalent configurations [25]. Therefore, extending the NCT method to accurately model such fluxional molecules is of significant interest. To address this challenge, we present an NCT implementation that operates directly on the three-dimensional Cartesian coordinates of the atoms, and apply it here to compute the eigenstates

of CH_5^+ . The code is available at <https://github.com/Callo42/nct-protonated-methane>.

II. METHODS

This section is organized as follows. First, we set up the nuclear Schrödinger equation. Second, we detail the NCT technique, covering the basis set, the construction of the target wavefunctions, the energy estimation procedure, and the optimization of the wavefunction ansatz. Finally, we compare the NCT method with other computational approaches for CH_5^+ calculations.

A. Hamiltonian

In this work, we perform a $J=0$ pure vibrational calculation for the ground and excited states of CH_5^+ by solving the time-independent Schrödinger equation for the nuclear Hamiltonian. All atomic coordinates throughout this work are defined in the Eckart frame [59], so that translational and rotational degrees of freedom have been removed. For conciseness, we denote the Eckart-fixed coordinates simply as \mathbf{x} . Under the Born–Oppenheimer approximation, the potential energy of the molecule is given by a function of its nuclear coordinates \mathbf{x} . Under these considerations, the Hamiltonian reads:

$$H = - \sum_{i,\alpha} \frac{1}{2m_i} \frac{\partial^2}{\partial x_{i\alpha}^2} + V(\mathbf{x}), \quad (1)$$

where m_i is the mass of the i -th atom and α is summed over three spatial dimensions. We use the ab initio-based, full-dimensional PES $V(\mathbf{x})$ that is fitted to 36,173 CCSD(T)/aug-cc-pVTZ calculations from Ref. [19]. As pointed out in Ref. [26], starting from normal coordinates is not sufficient for an accurate calculation of CH_5^+ . Therefore, we switch the coordinate system from the normal coordinates in our previous work [43] to the three-dimensional Cartesian coordinates.

B. Neural Canonical Transformation

In this study, we employ a normalizing flow [60, 61] model to realize the NCT. This method performs a unitary transformation on an initial basis to yield wavefunctions that incorporate physical interactions, such as anharmonic effects [55]. Consider the one-dimensional toy problem illustrated in Fig. 2. We begin with an orthonormal basis set composed of one-dimensional Hermite functions, $\{\Phi_n\}$, where n is the excitation number and each function is an eigenstate of a one-dimensional harmonic oscillator (HO). A neural network then parameterizes a bijective mapping from this simple basis to the set of true, anharmonic wavefunctions, $\{\Psi_n\}$. This transformation is constructed to preserve orthonormality while simultaneously introducing anharmonic effects into the final wavefunctions.

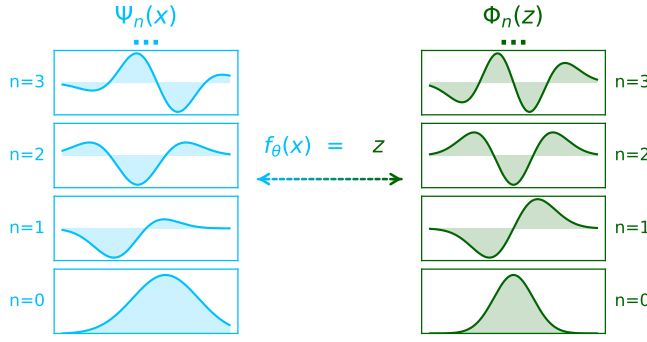


Figure 2. Neural Canonical Transformation: a sketch on a one-dimensional example. The $\Psi_n(x)$ in the left panel denotes the true wavefunction and the $\Phi_n(f_\theta(x))$ on the right refers to the wavefunction basis. $f_\theta(x)$ in the middle is the bijection parameterized by neural network that connects two sets of wavefunctions.

The NCT method employed in this work uses a framework similar to our previous study [43]. However, to properly describe the fluxional nature of CH_5^+ , we use Cartesian coordinates. The first step in calculating the eigenstates of the Hamiltonian in Eq. (1) is to define the wavefunction basis, $\{\Phi_n(z)\}$, in a latent space. This basis is constructed as the Hartree product of 18 one-dimensional HO wavefunctions:

$$\Phi_n(z) = \prod_{i=1}^{18} \phi_{n_i}(z_i), \quad (2)$$

where

$$\phi_{n_i}(z_i) = \frac{1}{\sqrt{2^{n_i} n_i!}} \left(\frac{m_i \omega_i}{\pi} \right)^{1/4} e^{-\frac{m_i \omega_i z_i^2}{2}} H_{n_i} \left(\sqrt{m_i \omega_i} z_i \right), \quad (3)$$

here $\mathbf{n} = (n_1, n_2, \dots, n_{18})$ is the vector of quantum numbers, and $\mathbf{z} = (z_1, z_2, \dots, z_{18})$ represents the coordinates in the 18-dimensional latent space. Each dimension i is associated with a mass m_i and a harmonic frequency ω_i . For our CH_5^+ calculation, the first three coordinates are assigned the mass of a carbon atom, while the remaining 15 are assigned the mass of a hydrogen atom. All calculations are performed in atomic units, with final results converted to other units, such as wavenumbers, where appropriate. In our setting, the variational calculation is carried out within an internal Hilbert subspace in which the overall translational and rotational motions are removed.

Each one-dimensional Hermite function in the latent space is initialized with respect to the global minimum configuration of the PES, which provides a good starting point for the variational optimization. The frequencies are set to treat identical atoms equally: the 15 oscillators corresponding to the hydrogen atoms are assigned a single frequency, ω_H , and the three oscillators for the carbon atom are assigned a different frequency, ω_C , where $\omega_C < \omega_H$. Since this initialization is in the latent space, it does not constrain the physical wavefunctions, which are determined by the learned normalizing flow. This construction defines our 18-dimensional wavefunction basis in the latent space. The quantum number vectors \mathbf{n}

of the basis functions are generated as follows: we enumerate all 18-dimensional non-negative integer vectors and sort them first by the total number of excitation quanta $\sum_{i=1}^{18} n_i$ in ascending order, and then in reverse-lexicographic order within each group of equal total quanta. The first entry $\mathbf{n} = \mathbf{0}$ corresponds to the ground state. We then truncate the sequence to the lowest N states.

Then a NCT is established to transform the wavefunction basis $\{\Phi_n(z)\}$ into the configuration space \mathbf{x} :

$$\Psi_n(\mathbf{x}) = \Phi_n(f_\theta(\mathbf{x})) \left| \det \left(\frac{\partial f_\theta(\mathbf{x})}{\partial \mathbf{x}} \right) \right|^{1/2}, \quad (4)$$

and the transformed wavefunctions $\{\Psi_n(\mathbf{x})\}$ span a variational subspace of the Hamiltonian [62]. In practice, before the coordinates are passed to the flow f_θ , they are re-projected onto the Eckart frame to ensure translational and rotational invariance of the wavefunction. During the transformation, it is expected that interactions such as collective dynamics of the atoms or anharmonicity are introduced into the wavefunction. Here, we parameterize f_θ using real-valued non-volume-preserving (RNVP) transformations [43, 63]. For conciseness, we abbreviate θ in the transformed wavefunction. The square root of the Jacobian determinant term, $\left| \det \left(\frac{\partial f_\theta(\mathbf{x})}{\partial \mathbf{x}} \right) \right|^{1/2}$, is introduced by the variable substitution process in normalizing flow and is the key factor that ensures the orthonormality of the transformed wavefunctions [43]:

$$\langle \Psi_n | \Psi_{n'} \rangle = \delta_{nn'}. \quad (5)$$

Then we estimate the energy levels of the Hamiltonian in Eq. (1) as:

$$E_{\mathbf{n}} = \langle \Psi_{\mathbf{n}} | H | \Psi_{\mathbf{n}} \rangle = \mathbb{E}_{\mathbf{x} \sim |\Psi_{\mathbf{n}}(\mathbf{x})|^2} [E_{\mathbf{n}}^{\text{loc}}(\mathbf{x})], \quad (6)$$

here, $\mathbb{E}[\cdot]$ denotes the expectation of the quantity inside the square brackets. The term $\langle \Psi_{\mathbf{n}} | H | \Psi_{\mathbf{n}} \rangle$ is the expectation value of the Hamiltonian for the eigenstate $\Psi_{\mathbf{n}}$. Finally, $E_{\mathbf{n}}^{\text{loc}}(\mathbf{x})$ denotes the local energy of the wavefunction [43]:

$$E_{\mathbf{n}}^{\text{loc}}(\mathbf{x}) = \sum_{i,\alpha} -\frac{1}{2m_i} \left[\frac{\partial^2}{\partial x_{i\alpha}^2} \ln |\Psi_{\mathbf{n}}(\mathbf{x})| + \left(\frac{\partial}{\partial x_{i\alpha}} \ln |\Psi_{\mathbf{n}}(\mathbf{x})| \right)^2 \right] + V(\mathbf{x}). \quad (7)$$

With access to the wavefunctions in Eq. (4), the energies in Eq. (6) are estimated by Markov chain Monte Carlo (MCMC) [64] sampling of the wavefunction. To restrict sampling to the $J=0$ pure vibrational subspace, the MCMC proposals are projected onto the Eckart frame, removing translational and rotational components from each proposed displacement (see the Supplementary Information for details).

To optimize the neural network parameters, we employ the ensemble Rayleigh–Ritz variational principle [43, 62, 65] and define the loss function as a Boltzmann-weighted sum of state energies:

$$\mathcal{L} = \sum_{\{\mathbf{n}\}} w_{\mathbf{n}} E_{\mathbf{n}}, \quad (8)$$

where the weights w_n are fixed Boltzmann factors at a chosen temperature T , determined by the harmonic-approximation vibrational energy levels $\varepsilon_n^{\text{harm}}$ obtained directly from the PES:

$$w_n = \frac{e^{-\beta \varepsilon_n^{\text{harm}}}}{\sum_{\{m\}} e^{-\beta \varepsilon_m^{\text{harm}}}}, \quad \beta = \frac{1}{k_B T}. \quad (9)$$

The harmonic levels $\varepsilon_n^{\text{harm}}$ are chosen as the lowest-lying levels up to the total number of states computed; they serve solely to set the weights and do not have a one-to-one correspondence with the actual excitation indices of the optimized wavefunctions. The Boltzmann weighting naturally assigns larger importance to lower-energy states, and minimizing \mathcal{L} yields the optimal variational estimate of the wavefunctions within the transformed subspace. Under this principle, once the optimal variational estimate is reached, each individual energy level E_n attains its best approximation simultaneously. In practice, we simultaneously solve for dozens of energy levels, and consequently, the summation in Eq. (8) typically involves a similar number of terms.

The gradient of the loss function with respect to the neural network parameters is estimated as [43, 54, 55]:

$$\nabla_{\theta} \mathcal{L} = 2 \sum_{\{n\}} w_n \mathbb{E}_{\mathbf{x} \sim [\Psi_n(\mathbf{x})]^2} [E_n^{\text{loc}}(\mathbf{x}) \nabla_{\theta} \ln |\Psi_n(\mathbf{x})|]. \quad (10)$$

We use the Adam [66] optimizer to perform gradient descent on the parameters. After convergence is reached, each energy level is measured following Eq. (6).

C. Comparison to Other Methods

The theoretical methods for CH_5^+ that have been discussed in Sec. I are valuable approaches that have had success in different areas. However, they still encounter various challenges. For instance, methods like VCI and iterative eigensolvers tend to need large basis sets for convergence, which can make scaling up the calculations to more excited states quite challenging. The superrotor and QG models, on the other hand, introduce several approximations to the PES, and combining different PES into the model can require considerable effort. DMC methods require manually constructing nodal surfaces under the fixed-node approximation, a process that depends on prior knowledge of the specific energy level. This dependence poses challenges for simultaneously computing multiple excited states, which is particularly important in the case of CH_5^+ . Compared to existing computational methods for the spectra of CH_5^+ , the NCT method stands out as an ab initio approach that readily and systematically scales to a large number of excited states and is able to seamlessly incorporate various PES.

III. RESULTS

This section is organized as follows. We begin in Sec. III A by describing the numerical details of our calculations. In

Sec. III B, we analyze the zero-point energy and radial distribution functions of the ground state. Next, Sec. III C presents the Lorentzian spectrum derived from the computed energy levels. Finally, Sec. III D reports our findings on relative similarity for various states.

A. Numerical Details

In this work, we carried out two calculations: the first involves a single calculation of the ground state, while the second targets the lowest 32 vibrational eigenstates (ground state plus 31 excited states) of the CH_5^+ nuclear Hamiltonian. All calculations were performed in atomic units for a system of one carbon and five hydrogen atoms (see Sec. II B). The RNVP [43, 63] network is initialized with 88,754 learnable parameters to ensure expressivity. The Adam [66] optimizer is set with a learning rate of 5×10^{-5} . For the ground-state calculation we use a total batch size of 6000 for steady convergence behavior. For excitation calculations, we train our model with 1200 batches per energy level, and we optimize for 10,000 iterations. For energy estimation of the ground state, we make an extra 100 iterations of Monte Carlo (MC) sampling of the converged wavefunctions, resulting in the equivalent of 600,000 samples. The zero-point energy is directly estimated on the sampled wavefunction. For excited states, we perform an extra 100 iterations of Monte Carlo sampling (equivalent to 120,000 samples per state) on the converged wavefunctions, and all eigenstates included in training are sampled simultaneously. For the radial distribution functions of C-H and H-H distances and the relative-similarity analysis to the three stationary points, we use the final converged checkpoint and sample each wavefunction individually.

B. Zero-point Energy and Radial Distribution Functions of Ground State

The zero-point energy we obtain is $10917.98(2.90) \text{ cm}^{-1}$, which agrees with the reference zero-point energy reported in the PES paper [19]. This agreement validates the adequacy of our computational setup for capturing the unique properties of this molecule. Without further architectural modification, we proceed to scale our calculation to excited states. In the following, we will illustrate that the NCT method successfully learns a delocalized wavefunction that explores the equivalent minima on the PES, capturing the fluxional nature of CH_5^+ .

The radial distribution functions of C-H distances and H-H distances of the ground state are shown in Fig. 3. The units of the C-H distances and the H-H distances are given in angstroms. The structure of CH_5^+ is learned by the wavefunction as the NCT method explores the PES.

The results show that the C-H distances form a wide unimodal distribution. This indicates that all the C-H bonds have significant flexibility in length, making it impossible to distinguish individual C-H bonds by bond length alone. The H-H distances form a bimodal distribution. The first peak occurs around 1.0 \AA with weak intensity, and the main peak takes

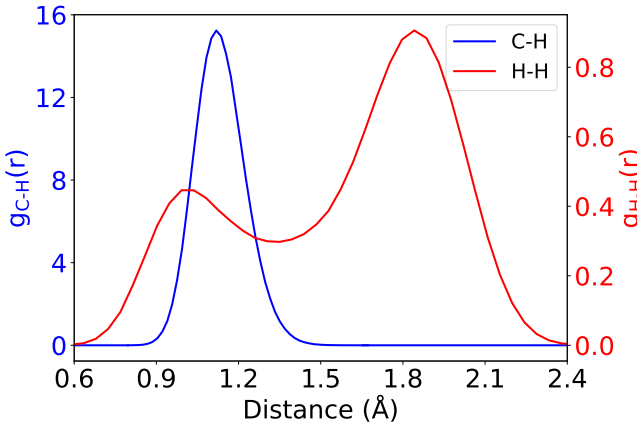


Figure 3. The radial distribution functions for C-H distances (in angstroms, left axis) and H-H distances (in angstrom, right axis) of the converged NCT wavefunction of ground state CH_5^+ .

place around 1.9 Å. The 1.0 Å peak indicates that there are a significant number of hydrogen pairs that are close to each other, forming the H_2 moiety. The 1.9 Å peak is formed by other hydrogen pairs. The unimodal C-H distances and bimodal H-H distances confirm that the quantum ground state is dominated by CH_3^+ and H_2 , which is also consistent with previous studies in Ref. [2, 18, 23].

C. Excited States and Lorentzian Spectrum

The excited-state energy levels from the 32-state CH_5^+ calculation are listed in Table S1, in which the zero-point energy is omitted and the 31 excited states are reported as relative energy differences to the zero-point energy in cm^{-1} . In addition, we also calculate the lowest 24 excited energy levels of CH_4 using the NCT method with the PES from Ref. [37]. We have verified that performing the CH_4 calculation in the Eckart frame with Cartesian coordinates yields results consistent with those obtained using normal coordinates. Since the normal-coordinate formulation is the standard approach for CH_4 , we present only the normal-coordinate results here, following the same scheme in Ref. [43].

In contrast to the IR spectrum reported in Ref. [21], which includes broadening from IR intensities, our approach generates a spectrum by directly broadening the calculated energy levels with equal weight for each level. To achieve this, we apply a Lorentzian convolution with a full width at half maximum of 30 cm^{-1} to both our calculated NCT energy levels and the levels from harmonic approximations, as shown in Fig. 4. The harmonic approximation results for CH_5^+ are from the normal mode frequencies in Ref. [19] and include only fundamental levels above 900 cm^{-1} because the low-frequency levels are highly anharmonic [21]. The harmonic results for CH_4 are from the harmonic approximation of the PES in Ref. [37].

In comparison to the harmonic approximations of CH_5^+ and the NCT result of CH_4 , the Lorentzian spectrum of CH_5^+ displays notable discrepancies in several frequency regions. At

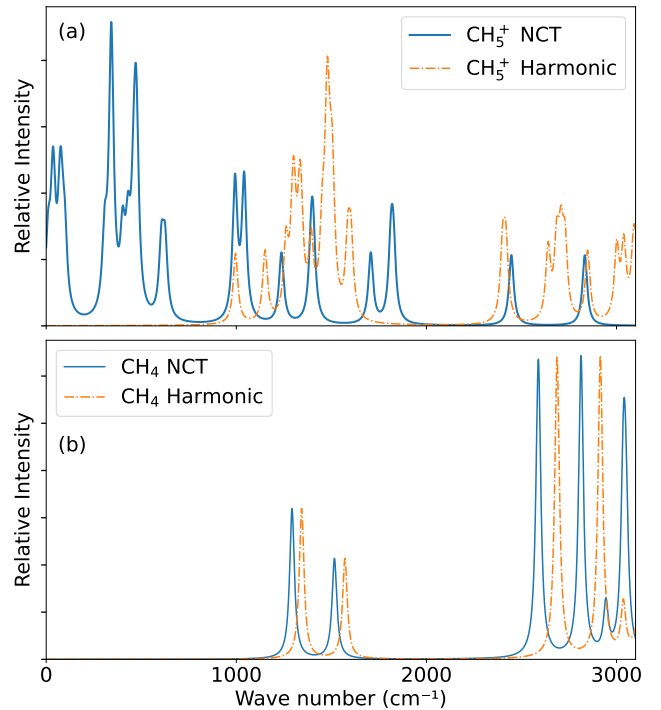


Figure 4. The Lorentzian spectra of the energy levels (convolved with FWHM of 30 cm^{-1}) for (a) CH_5^+ and (b) CH_4 from the NCT calculation and their harmonic approximations. The harmonic approximation result of CH_5^+ is from the normal mode frequencies in Ref. [19]. The harmonic results for CH_4 are from the PES in Ref. [37].

low frequencies, numerous levels appear with the lowest excitation around 10 cm^{-1} , observed exclusively in the NCT spectrum of CH_5^+ . These levels arise from strong anharmonicity and are generally absent in experimental spectra due to limited sensitivity in this domain, as demonstrated by the laser-induced reaction spectrum of Ref. [4]. No corresponding states are present in the more rigid CH_4 molecule. Near 2000 cm^{-1} , CH_5^+ has additional energy levels in a region forbidden by the harmonic approximation. The DMC method can also identify states within this region, provided the nodal surface is chosen properly. For example, Ref. [24] reports a high-symmetry state at 2164 cm^{-1} found by DMC. However, due to the symmetry, such a state is generally forbidden or exhibits only negligible intensity in the IR spectrum.

In the CH_4 molecule, atomic vibrations are confined near the equilibrium configuration. This gives rise to sharp and isolated spectral peaks for each normal mode. The NCT results primarily manifest as red shifts of the harmonic energy levels, in agreement with the findings of Ref. [37]. In contrast, the spectrum of CH_5^+ differs markedly from its harmonic approximation, exhibiting numerous low-energy excitations that reflect the large anharmonicity, as revealed by the NCT method. We will illustrate later that the wavefunctions of both the low-energy and high-energy excited states exhibit significant delocalization over the equivalent minima on the PES.

D. Relative Similarity to three Stationary Points

For each chosen state, we first sample the converged wavefunction to generate 120,000 samples. From these samples, we calculate the root mean square deviation (RMSD) with respect to each of the three stationary points. We then take the reciprocals of these RMSD values and, finally, normalize them to measure the relative similarity of each state to the stationary points, as illustrated in Fig. 5. For illustration, we choose the ground state, the first excited state at 9.7 cm^{-1} , and two additional excited states with energy levels of 34.3 cm^{-1} and 2832.8 cm^{-1} .

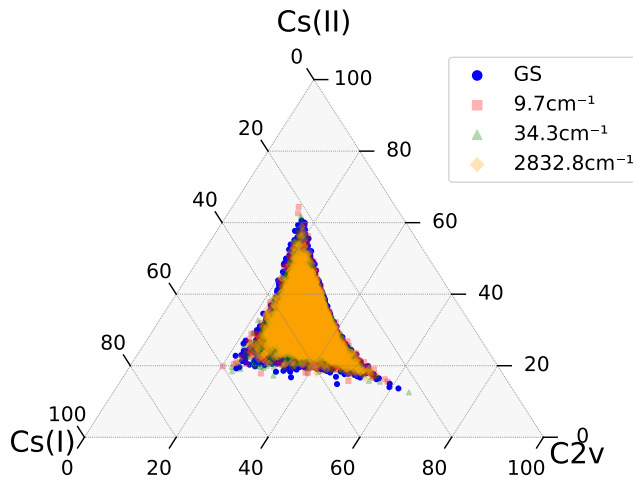


Figure 5. Ternary diagram of the relative similarity of samples from each state to the three types of stationary point configurations on PES. The values are percentages and are normalized for each sample.

The ground-state and excited-state distributions exhibit a common feature: both are centered and form three peaks directed toward the stationary points. This structure indicates a balanced preference for the $C_s(I)$, $C_s(II)$ and C_{2v} stationary points. Because the molecule in these states has a similar preference for each configuration, there is a significant probability of finding it in any of them. This probability signifies a delo-

calized wavefunction, which in turn allows the molecule to move among these three configurations.

IV. DISCUSSIONS

Strong anharmonicity and large-amplitude motions of hydrogen atoms in CH_5^+ give rise to numerous low-energy excitations, which constitute the most distinctive spectral feature of this molecule. The NCT wavefunction is capable of expressing the delocalization of the nuclear wavefunction, thereby capturing the fluxional nature of CH_5^+ . We find that the nuclear ground state, as well as the low-lying and high-energy excited states, are highly anharmonic and exhibit similar preferences for the three stationary points on the PES.

This work extends the applications of the NCT method to fluxional molecules, enabling it to solve eigenstates with delocalized wavefunctions for systems that undergo large-amplitude spatial motion, such as CH_5^+ . Using the NCT method, we present a variational approach that solves the nuclear Schrödinger equation for CH_5^+ . The method scales linearly with the number of excited states. Finally, in future studies, we expect to enforce the correct hydrogen-permutation symmetry on the wavefunction to obtain more accurate energy levels. A permutation-equivariant implementation of the flow model is necessary to achieve this, as demonstrated in Ref. [67].

ACKNOWLEDGMENTS

We gratefully thank Tucker Carrington Jr. for providing the potential energy surface of protonated methane. We are grateful for the useful discussions with Hao Xie, Xinguo Ren, Xin-Yang Dong, Lu Zhao, Zi-Hang Li, Zhen-Dong Cao, Shi-Gang Ou and Bei Qiao. This work is supported by the National Natural Science Foundation of China under Grants No. 92270107, No. T2225018, No. 12188101, No. T2121001 and the Strategic Priority Research Program of the Chinese Academy of Sciences under Grants No. XDB05000000, and the National Key Projects for Research and Development of China Grants No. 2021YFA1400400.

[1] P. R. Schreiner, S.-J. Kim, H. F. Schaefer, and P. Von Ragué Schleyer, *The Journal of Chemical Physics* **99**, 3716 (1993).

[2] D. Marx and M. Parrinello, *Nature* **375**, 216 (1995).

[3] D. Marx and M. Parrinello, *Science* **284**, 59 (1999).

[4] O. Asvany, P. K. P. B. Redlich, I. Hegemann, S. Schlemmer, and D. Marx, *Science* **309**, 1219 (2005).

[5] G. A. Olah, N. Hartz, G. Rasul, and G. S. Prakash, *Journal of the American Chemical Society* **117**, 1336 (1995).

[6] G. A. Olah and G. Rasul, *Accounts of chemical research* **30**, 245 (1997).

[7] E. Herbst, S. Green, P. Thaddeus, and W. Klemperer, *Astrophysical Journal* **215**, 503 (1977).

[8] D. Talbi and R. Saxon, *Astronomy and Astrophysics* (ISSN 0004-6361), vol. 261, no. 2, p. 671-676. **261**, 671 (1992).

[9] V. Tal'roze, in *Doklady Akad. Nauk SSSR*, Vol. 86 (1952) p. 909.

[10] E. T. White, J. Tang, and T. Oka, *Science* **284**, 135 (1999).

[11] O. Asvany, K. M. T. Yamada, S. Brünken, A. Potapov, and S. Schlemmer, *Science* **347**, 1346 (2015).

[12] S. Brackertz, S. Schlemmer, and O. Asvany, *Journal of Molecular Spectroscopy* **342**, 73 (2017).

[13] T. Oka, *Science* **347**, 1313 (2015).

[14] P. Bunker, B. Ostojić, and S. Yurchenko, *Journal of Molecular Structure* **695-696**, 253 (2004).

[15] A. Brown, B. J. Braams, K. Christoffel, Z. Jin, and J. M. Bowman, *The Journal of Chemical Physics* **119**, 8790 (2003).

[16] A. B. McCoy, B. J. Braams, A. Brown, X. Huang, Z. Jin, and J. M. Bowman, *The Journal of Physical Chemistry A* **108**, 4991 (2004).

[17] A. Brown, A. B. McCoy, B. J. Braams, Z. Jin, and J. M. Bowman, *The Journal of Chemical Physics* **121**, 4105 (2004).

[18] K. C. Thompson, D. L. Crittenden, and M. J. T. Jordan, *Journal of the American Chemical Society* **127**, 4954 (2005).

[19] Z. Jin, B. J. Braams, and J. M. Bowman, *The Journal of Physical Chemistry A* **110**, 1569 (2006).

[20] X. Huang, L. M. Johnson, J. M. Bowman, and A. B. McCoy, *Journal of the American Chemical Society* **128**, 3478 (2006).

[21] X. Huang, A. B. McCoy, J. M. Bowman, L. M. Johnson, C. Savage, F. Dong, and D. J. Nesbitt, *Science* **311**, 60 (2006).

[22] L. M. Johnson and A. B. McCoy, *The Journal of Physical Chemistry A* **110**, 8213 (2006).

[23] C. E. Hinkle and A. B. McCoy, *The Journal of Physical Chemistry A* **112**, 2058 (2008).

[24] C. E. Hinkle and A. B. McCoy, *The Journal of Physical Chemistry A* **113**, 4587 (2009).

[25] X.-G. Wang and T. Carrington, *The Journal of Chemical Physics* **129**, 234102 (2008).

[26] X. Wang and T. Carrington (Kos, Greece, 2015) pp. 336–337.

[27] X.-G. Wang and T. Carrington, *The Journal of Chemical Physics* **144**, 204304 (2016).

[28] C. Fábris, M. Quack, and A. G. Császár, *The Journal of Chemical Physics* **147**, 134101 (2017).

[29] R. Wodraszka and U. Manthe, *The Journal of Physical Chemistry Letters* **6**, 4229 (2015).

[30] H. Schmiedt, P. Jensen, and S. Schlemmer, *Physical Review Letters* **117**, 223002 (2016).

[31] H. Schmiedt, P. Jensen, and S. Schlemmer, *Chemical Physics Letters* **672**, 34 (2017).

[32] C. Fábris and A. G. Császár, *Physical Chemistry Chemical Physics* **20**, 16913 (2018).

[33] J. I. Rawlinson, *The Journal of Chemical Physics* **151**, 164303 (2019).

[34] J. I. Rawlinson, C. Fábris, and A. G. Császár, *Chemical Communications* **57**, 4827 (2021).

[35] I. Simkó, C. Fábris, and A. G. Császár, *Journal of Chemical Theory and Computation* **19**, 42 (2023).

[36] D. Gray and A. Robiette, *Molecular Physics* **37**, 1901 (1979).

[37] T. J. Lee, J. M. L. Martin, and P. R. Taylor, *The Journal of Chemical Physics* **102**, 254 (1995).

[38] E. B. Wilson, J. C. Decius, P. C. Cross, and B. R. Sundheim, *Journal of The Electrochemical Society* **102**, 235C (1955).

[39] S. Carter, H. M. Shnider, and J. M. Bowman, *The Journal of Chemical Physics* **110**, 8417 (1999).

[40] S. Carter and J. M. Bowman, *The Journal of Physical Chemistry A* **104**, 2355 (2000).

[41] K. Momma and F. Izumi, *Journal of Applied Crystallography* **44**, 1272 (2011).

[42] J. M. Bowman, T. Carrington, and H.-D. Meyer, *Molecular Physics* **106**, 2145 (2008).

[43] Q. Zhang, R.-S. Wang, and L. Wang, *The Journal of Chemical Physics* **161**, 024103 (2024).

[44] K. Ishii, T. Shimazaki, M. Tachikawa, and Y. Kita, *Chemical Physics Letters* **787**, 139263 (2022).

[45] Y. Saleh, Á. Fernández Corral, E. Vogt, A. Iske, J. Küpper, and A. Yachmenev, *Journal of Chemical Theory and Computation*, *acs.jctc.5c00590* (2025).

[46] R. Han, R. Ketkaew, and S. Luber, *The Journal of Physical Chemistry A* **126**, 801 (2022).

[47] S. Manzhos and T. Carrington, *Chemical Reviews* **121**, 10187 (2021).

[48] S. Manzhos, M. Ihara, and T. Carrington, in *Quantum Chemistry in the Age of Machine Learning* (Elsevier, 2023) pp. 355–390.

[49] H. Ren, H. Li, Q. Zhang, L. Liang, W. Guo, F. Huang, Y. Luo, and J. Jiang, *Fundamental Research* **1**, 488 (2021).

[50] D. Shanavas Rasheeda, A. Martín Santa Daría, B. Schröder, E. Mátyus, and J. Behler, *Physical Chemistry Chemical Physics* **24**, 29381 (2022).

[51] B. Han, R. Okabe, A. Chotrattanapituk, M. Cheng, M. Li, and Y. Cheng, *Digital Discovery* **4**, 584 (2025).

[52] R. J. DiRisio, F. Lu, and A. B. McCoy, *The Journal of Physical Chemistry A* **125**, 5849 (2021).

[53] F. Lu, L. Cheng, R. J. DiRisio, J. M. Finney, M. A. Boyer, P. Moonkaen, J. Sun, S. J. R. Lee, J. E. Deustua, T. F. Miller, and A. B. McCoy, *The Journal of Physical Chemistry A* **126**, 4013 (2022).

[54] H. X. Hao Xie, L. Z. Linfeng Zhang, and L. W. Lei Wang, *Journal of Machine Learning* **1**, 38 (2022).

[55] H. Xie, L. Zhang, and L. Wang, *SciPost Physics* **14**, 154 (2023).

[56] Z. Li, H. Xie, X. Dong, and L. Wang, *Deep variational free energy calculation of hydrogen hugoniot* (2025), *arXiv:2507.18540* [cond-mat.str-el].

[57] Q. Zhang, X. Wang, R. Shi, X. Ren, H. Wang, and L. Wang, *Neural Canonical Transformations for Quantum Anharmonic Solids of Lithium* (2024), version Number: 2.

[58] Q. Zhang and L. Wang, *Quantum anharmonic effects in hydrogen-bond symmetrization of high-pressure ice* (2025), *arXiv:2507.01452* [cond-mat.mtrl-sci].

[59] C. Eckart, *Physical Review* **47**, 552.

[60] G. Papamakarios, E. Nalisnick, D. J. Rezende, S. Mohamed, and B. Lakshminarayanan, *Normalizing Flows for Probabilistic Modeling and Inference* (2021), *arXiv:1912.02762* [stat].

[61] I. Kobyzev, S. J. Prince, and M. A. Brubaker, *IEEE Transactions on Pattern Analysis and Machine Intelligence* **43**, 3964 (2021).

[62] R. Courant and D. Hilbert (Wiley-VCH, Weinheim, 2009) num Pages: 456.

[63] L. Dinh, J. Sohl-Dickstein, and S. Bengio, *Density estimation using Real NVP* (2017), *arXiv:1605.08803* [cs].

[64] F. Becca and S. Sorella, *Quantum Monte Carlo approaches for correlated systems* (Cambridge university pres, Cambridge New York, 2017).

[65] E. K. U. Gross, L. N. Oliveira, and W. Kohn, *Physical Review A* **37**, 2805 (1988).

[66] D. P. Kingma and J. Ba, *Adam: A Method for Stochastic Optimization* (2014), *arXiv:1412.6980* [cs].

[67] P. Wirnsberger, A. J. Ballard, G. Papamakarios, S. Abercrombie, S. Racanière, A. Pritzel, D. Jimenez Rezende, and C. Blundell, *The Journal of Chemical Physics* **153**, 144112 (2020).

Appendix: Supplementary Information

1. Eckart-Consistent MCMC Sampling

In the main text, the MCMC sampling is performed in the $J=0$ pure vibrational subspace. This is achieved by constructing proposals that live entirely within the Eckart frame [59], a body-fixed coordinate system that decouples internal vibrational motion from overall translation and rotation.

Consider an N -atom molecule with masses $\{m_i\}_{i=1}^N$ and lab-frame positions $\{\mathbf{r}_i \in \mathbb{R}^3\}$. Fix a reference configuration $\{\mathbf{r}_i^0\}$ (typically an equilibrium geometry). Define the center-of-mass (COM) position $\mathbf{R}_{\text{cm}} = M^{-1} \sum_i m_i \mathbf{r}_i$ with total mass $M = \sum_i m_i$, and the COM-centered coordinates

$$\mathbf{x}_i = \mathbf{r}_i - \mathbf{R}_{\text{cm}}, \quad \mathbf{q}_i = \mathbf{r}_i^0 - \mathbf{R}_{\text{cm}}^0, \quad (\text{S1})$$

where \mathbf{x}_i denotes the COM-centered position of atom i in the current configuration and \mathbf{q}_i denotes that in the reference.

The Eckart frame is obtained by finding the rotation R_* that best aligns the current configuration to the reference in the mass-weighted metric:

$$R_* = \arg \min_R \sum_{i=1}^N m_i \|\mathbf{x}_i R - \mathbf{q}_i\|^2. \quad (\text{S2})$$

The Eckart-fixed coordinates are then $\mathbf{y}_i = \mathbf{x}_i R_*$, which satisfy the Eckart rotational condition $\sum_i m_i \mathbf{q}_i \times \mathbf{y}_i = \mathbf{0}$. In practice, the optimal rotation is computed via the singular value decomposition of the 3×3 mass-weighted correlation matrix $C = \sum_i m_i \mathbf{x}_i^\top \mathbf{q}_i$. Writing $C = U \Sigma V^\top$, the optimal rotation is $R_* = U V^\top$.

Eckart-consistent MCMC proposal: To sample the wavefunction in the Eckart gauge, we construct proposals that contain no net translational or rotational displacement. Working in stacked mass-weighted coordinates $\delta \mathbf{Q} \in \mathbb{R}^{3N}$ with atom-wise blocks $\delta \mathbf{Q}_i = \sqrt{m_i} \delta \mathbf{y}_i$, the rigid-body directions at the reference are

$$\delta \mathbf{Q}_i^{(T,a)} = \sqrt{m_i} \mathbf{e}_a, \quad (\text{S3})$$

$$\delta \mathbf{Q}_i^{(R,a)} = \sqrt{m_i} (\mathbf{e}_a \times \mathbf{q}_i), \quad (\text{S4})$$

for $a = x, y, z$, where \mathbf{e}_a are the Cartesian unit vectors. Let $B \in \mathbb{R}^{3N \times k}$ ($k \leq 6$) have orthonormal columns spanning these rigid-body directions. The projector onto the internal (vibrational) subspace is

$$P_{\text{int}} = I - B B^\top. \quad (\text{S5})$$

The proposal proceeds as follows: (i) draw an isotropic Gaussian displacement $\delta \mathbf{Q} \sim \mathcal{N}(0, \sigma^2 I_{3N})$; (ii) project out rigid-body components, $\delta \mathbf{Q}_{\text{int}} = P_{\text{int}} \delta \mathbf{Q}$; (iii) convert to Cartesian displacements, $\delta \mathbf{y}_i = \delta \mathbf{Q}_{\text{int},i} / \sqrt{m_i}$; (iv) propose $\mathbf{y}'_i = \mathbf{y}_i + \delta \mathbf{y}_i$.

The projection guarantees $\sum_i m_i \delta \mathbf{y}_i = \mathbf{0}$ (no COM drift) and $\sum_i m_i \mathbf{q}_i \times \delta \mathbf{y}_i = \mathbf{0}$ (no infinitesimal rotation), so the proposal remains in the Eckart gauge. Moreover, because P_{int} is a symmetric projector and the base draw is isotropic, the projected increment has an even distribution, yielding a symmetric proposal $q(\mathbf{y}' \mid \mathbf{y}) = q(\mathbf{y} \mid \mathbf{y}')$. The Metropolis–Hastings acceptance ratio thus reduces to the standard Metropolis form:

$$\alpha(\mathbf{y} \rightarrow \mathbf{y}') = \min\left(1, \frac{|\Psi(\mathbf{y}')|^2}{|\Psi(\mathbf{y})|^2}\right). \quad (\text{S6})$$

Table S1. The energy levels of all 31 excited states from the 32-state NCT calculation. The energy levels are in units of cm^{-1} . The zero-point energy is omitted and all excited states are reported as relative energy differences from the zero-point energy. Each state is measured with the equivalent of 120,000 samples (see text for details).

number	NCT Energy	number	NCT Energy	number	NCT Energy
1	9.7(0.1)	12	402.1(0.3)	23	1042.0(0.4)
2	34.3(0.2)	13	430.0(0.3)	24	1237.2(0.3)
3	38.2(0.2)	14	459.8(0.3)	25	1394.6(0.4)
4	71.9(0.2)	15	468.6(0.3)	26	1404.2(0.3)
5	79.1(0.2)	16	473.9(0.3)	27	1707.2(0.3)
6	97.2(0.2)	17	476.1(0.3)	28	1813.4(0.4)
7	307.5(0.2)	18	606.2(0.3)	29	1825.8(0.4)
8	341.6(0.3)	19	625.3(0.2)	30	2446.8(0.3)
9	342.0(0.2)	20	991.1(0.4)	31	2832.8(0.3)
10	342.9(0.2)	21	995.1(0.4)		
11	343.3(0.2)	22	1040.4(0.3)		